Effect of Thermal Cycling on Friction Stir Welds of 2195 Aluminum Alloy

Postweld thermal cycling of friction stir aluminum alloy welds leads to complex microstructural evolution

BY G. OERTELT, S. S. BABU, S. A. DAVID AND E. A. KENIK

ABSTRACT. The microstructure in friction stir welded (FSW) aluminum Alloy 2195 was investigated in the as-welded and postweld thermal cycled conditions. The as-welded microstructure in the dynamically recrystallized zone (DXZ) contains both dislocated and recovered grains. This DXZ region was subjected to thermal cycling. Thermal cycling led to a decrease in dislocation density and precipitation of the second phase within and along the grain boundaries. These results show the DXZ region is supersaturated with alloying element. The grain growth kinetics in the DXZ region were complicated because of the interaction of precipitation and the recovery of deformed grains.

Introduction

Friction stir welding (FSW) involves plunging a rotating shouldered pin tool into the faying surface of two plates and traversing the tool along its length (Ref. 1). Welding, which is in solid state, is achieved by plastic flow of frictionally heated material. Extensive research has been accomplished on developing the friction stir welding process for aluminum alloys used in aerospace applications (Refs. 2–6). The process has been applied to both precipitation-strengthened (Refs. 1–9) and nonprecipitation-strengthened aluminum alloys (Ref. 10). Even Alloy 7075 (Al-Zn-Mg type), which is considered difficult to weld with conventional welding processes, was successfully welded with FSW and exhibited good properties (Ref. 7). In addition, friction stir welds of 5454 (Al-Mg) alloys have shown potentially good corrosion properties (Ref. 10). Results of these investigations show the FSW process yields better properties than conventional welding processes for aluminum alloys.

The details of the microstructural evolution during the severe thermomechanical conditions imposed by this welding process are far from being completely understood. For example, the grains in the dynamically recrystallized zone are not completely recrystallized and there exists a high density of dislocations within these grains (Ref. 6). The precipitation of various phases may also complicate the microstructural evolution; these precipitation reactions are determined by the initial state of the base metal (Ref. 8) and alloy composition. In addition, the precipitation characteristics may influence the final grain size of these welds. Besides the microstructural evolution during welding, the stability of the microstructure during subsequent heat treatment is also not understood. In particular, the response of DXZ microstructure to another weld thermal cycle is not known. This subsequent weld thermal cycle may be due to repair welding or subsequent weld overlaps. In addition, the stability of this microstructure during high-temperature exposure is not known. In particular, the initial state of the DXZ may affect the grain growth characteristics. Therefore, in this work, microstructural evolution in the DXZ, stability of the microstructure to multiple thermal cycles and grain growth characteristics of DXZ regions were investigated in friction stir welds of 2195 aluminum alloy.

KEY WORDS

Friction Stir Welding
Aluminum Alloy 2195
Postweld Thermal Cycling
Dynamically Recrystallized Zone
Thermomechanically Affected Zone
Heat-Affected Zone

Experimental

Aluminum Alloy 2195 (Al-4.0 wt-% Cu-1.0% Li-0.5% Mg-0.4% Ag-0.1% Zr) was used in this investigation, and the plate was in the T8 (solution treated, cold worked and artificially aged) condition (Refs. 6, 11) before the FSW operation. The friction stir welding was done at the Lockheed Martin Manned Space System Complex, New Orleans, La. The 5.8-mm-thick (0.23-in.) plates were friction stir welded with the following process parameters: 10.9-mm (0.43-in.) pin-tool diameter; 7.9-mm (0.31-in.) pin-tool height; 0.18-mm (0.007-in.) penetration ligament; 27.9-mm (1.1-in.) shoulder diameter; 200–250 rpm pin-tool rotation speed; 1.59 mm/s (3.75 in./min) welding speed. Samples were cut from the welds along the transverse direction. The DXZ regions in these samples were subjected to postweld thermal cycling using a Gleeble® thermomechanical simulator. The particulars of this thermal cycle are given in the Result section of this paper. Long-term grain growth behavior was investigated by subjecting the DXZ regions to thermal aging at 200, 300 and 400°C in a furnace for different times.

The samples were characterized with standard optical microscopy. The grain size measurements were performed on scanned images of optical micrographs using the public domain NIH image program (developed at the U.S. National Institute of Health and available on the Internet at *http://rsb.info.nih.gov/nih-image/*). Backscattered electron imaging was performed with a Philips XL30/FEG scanning electron microscope

G. OERTELT is with the University of Leoben, Leoben, Austria. S. S. BABU, S. A. DAVID and E. A. KENIK are with the Metals and Ceramics Division, Oak Ridge National Laboratory, Oak Ridge, Tenn.

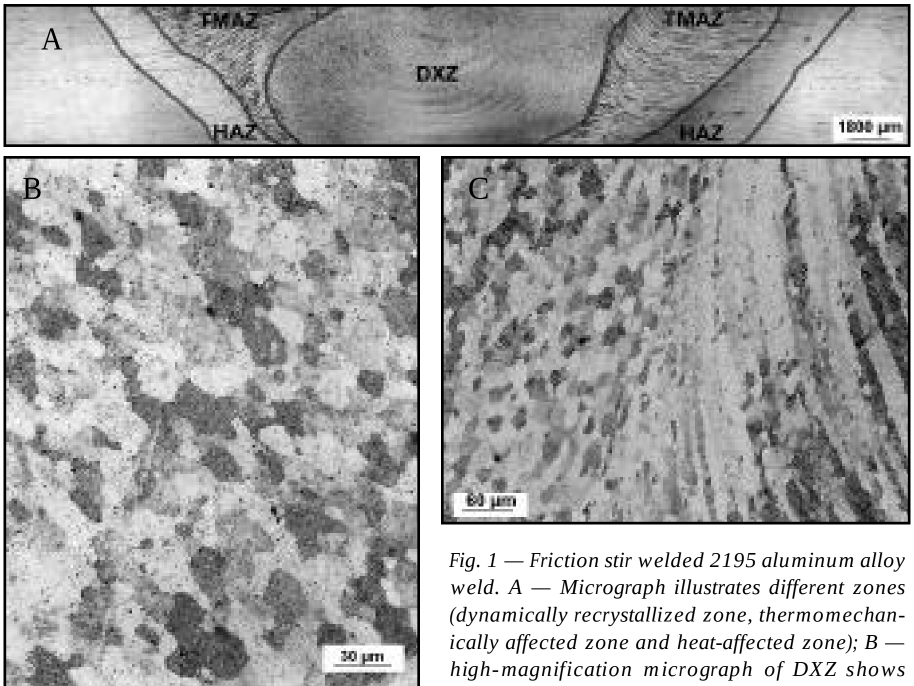

Fig. 1 — Friction stir welded 2195 aluminum alloy weld. A — Micrograph illustrates different zones (dynamically recrystallized zone, thermomechanically affected zone and heat-affected zone); B — high-magnification micrograph of DXZ shows equiaxed grains; C — leading edge of DXZ and TMAZ (right side of the micrograph in A) shows a sharp change in equiaxed to elongated orientation.

Table 1 — Raw Data from the Image Analysis of Precipitates from SEM Micrographs from the As-Welded and after TC1 Treatment. (Numbers for Precipitates and area percent are given.)

	As-Welded		TC1	
Frame	Number	Percent	Number	Percent
1	48	1.082	131	5.114
2	137	2.261	108	5.849
3	73	2.948	99	7.196
4	65	1.191	155	6.24
5	87	1.838	119	5.118
6	38	0.778	122	3.601
7	97	2.465	173	5.05
8	93	1.593	126	6.38
9	111	2.744	84	3.281
10	76	1.696	93	5.664
Average		1.8606 ±.731		5.349 ± 1.209

(SEM) to analyze coarse second-phase precipitates. The precipitate volume fractions in these images were also measured with the NIH image analyzer program. Transmission electron microscopy (TEM) was performed with a Philips CM12 microscope to evaluate the recovered structures and precipitates in the weld. Hardness variations across the weld were measured using a LECO M-400 H2 microhardness tester.

Results and Discussions

As-Welded Microstructure

The macrostructure of the 2195 aluminum alloy weld is shown in Fig. 1A. The macrograph indicates three distinct regions of the weld: dynamically recrystallized zone (DXZ), thermomechanically affected zone (TMAZ) and heat-affected zone (HAZ). The macrograph shows the lack of symmetry along the centerline of the weld. This is attributed to the nature of the plasticized metal movement around the rotating tool during welding. The micrograph in Fig. 1B shows primarily equiaxed grain structure in the DXZ region. The sharp boundary between the DXZ and the leading edge of the TMAZ is shown in Fig. 1C. These results are consistent with other published work on FSW (Refs. 3, 6). In order to compare the microstructure in the DXZ region with that of the base metal (BM), SEM and TEM characterizations of the base metal were also performed — Fig. 2. The backscattered SEM image with EDS analysis indicated a small number of Cu-rich and Cu-Fe-rich precipitates (<0.5 µm) in the base metal region. The reasons for the presence of Fe in these precipitates are not known. TEM characterization with electron diffraction showed the presence of very fine T1 (Al_2CuLi type, ~50 nm long and ~1 nm thick) precipitates.

The DXZ contained a fine grain structure, including Cu-rich and Cu-Fe-rich precipitates along the grain boundaries — Fig. 3B. In general, the Cu-Fe-rich precipitates were coarser than the Cu-rich precipitates. The SEM analysis at high magnification showed small precipitates within the grain — Fig. 3C. It is speculated these are the same precipitates observed in the base metal region, which might have undergone some coarsening during friction stir welding. The EDS spectrum from the matrix showed the presence of copper in the matrix (Fig. 3D) and indicates some copper supersaturation in the matrix. Therefore, on thermal cycling, the precipitation reaction is expected. The presence of Cu and Fe in the grain boundary precipitates is supported by EDS analysis — Fig. 3E. The micrograph in Fig. 3C shows the precipitate fraction is higher than that of the base metal region. This indicates thermal cycles experienced by the metal during the friction stir welding process are sufficient to initiate precipitation reactions within the grains and along the grain boundaries.

Transmission electron micrographs of the DXZ are shown in Fig. 4. Interestingly, dislocation networks were observed within the grain — Fig. 4A. The electron diffraction indicated the absence of T1 precipitates. These results are in agreement with the published literature (Ref. 6). Off-zone imaging (Fig. 4B) and EDS analysis of some of the grains indicated the presence of small Cu-rich precipitates within grains and along the grain boundaries. Note these precipitates are smaller than those observed in the SEM. Based on previous literature (Ref. 6), these precipitates are expected to be equilibrium (Al_7Cu_4Li-type) T_B precipitates. The present characterization did not detect any β' (Al_3Zr) precipitates in the DXZ. The TEM characterization of the DXZ region also indicated there are grains in the process of recovery (Fig. 4C) adjacent to grains that exhibit large dislocation density. The micrograph shows a grain with dislocations aligning to form a subgrain boundary, and this grain did not exhibit extensive dislocation networks as shown in Fig. 4A. Such microstructural features were not previously reported, and it is interesting to note that grains with different degrees of recovery exist next to each other. This phenomena cannot be attributed to differences in thermal cycles because of the large thermal conductivity of aluminum alloys. Li, *et al.*, attributed the observed high-dislocation density in the grains to possible deformation by the friction stir welding tool shoulder and metal interactions (Ref. 6). If that were the case, the dislocation density would be uniform throughout all the grains in certain regions and it would be absent away from the shoulder tool. The observed dislocation density differences in the current welds are for neighboring grains. Therefore, the observed phenomena may be attributed to deformation gradients across the grains during the welding operation. This speculation is supported by the results of a detailed computational model with meso-scale plastic deformation, recovery and recrystallization models (Ref. 12) subjected to nonuniform deformation.

The above-mentioned microstructural observations showed the DXZ region essentially consists of grains at different stages of the recovery process. Moreover, almost all the grains had Cu-rich precipitates along the grain boundary and within the grain.

Effect of Thermal Cycling on Microstructure Development

The stability of the DXZ region in friction stir welds to subsequent thermal cycling was evaluated. Samples were cut in the transverse direction, as shown in Fig. 5A, and subjected to two sets of thermal cycles (Fig. 5B) in a Gleeble® thermomechanical simulator. Experiments were designed so that the DXZ region was heated to peak temperature by adjusting the copper jaws that restrain the sample in the Gleeble instrument. As a result, the uniform temperature zone was centered on the DXZ region; its thermal cycles are shown in Fig. 5B. In the first stage (TC1), the DXZ was heated to 430°C and cooled continuously. That thermal cycle represents a typical one experienced by the DXZ region during FSW (Refs. 3, 13). The reason for this thermal cycle was to evaluate the effect of subsequent FSW passes on the previously formed DXZ. In the second stage, to consider the effects of multiple passes, the TC1 samples were subjected to an additional thermal cycle (TC2) similar to that of TC1.

Hardness variations across the DXZ are compared in Fig. 5C. The plots also show the hardness in the TMAZ, HAZ and BM regions. Hardness across the DXZ regions decreases from 122 to 106 VHN after TC1. But the additional TC2 did not result in a significant further drop in hardness. It is interesting to note hardness after TC1 is similar to that of the HAZ. Hardness in the TMAZ, HAZ and BM reduced slightly, since they were not subjected to high temperature. The results show the thermal cycles do reduce the hardness and the reduction is essentially complete after TC1. Therefore, the microstructure after TC1 was characterized with SEM and TEM. The backscattered electron image of the DXZ region subjected to TC1 cycle is shown in Fig. 6A. The grain size of the samples remained the same in these alloys. The microstructure exhibited extensive grain boundary precipitation and small precipitates were also observed within the grains — Fig. 6B. An image analysis of all the precipitates (Table 1) showed the volume percentage of precipitates in the TC1 condition (5.35%) is higher than that of the as-welded (1.86%) condition. The nature of dislocation content and precipitation were also evaluated with TEM. The TEM micrograph and electron diffraction showed the absence of T1 precipitates — Fig. 6C. However, extensive dislocation networks were absent in this condition, except for small loops. Detailed analysis showed Cu-rich precipitate within and along the grains. Some of these small precipitates were rich in Cu and Ag — Fig. 6D. In some areas, coarse composite precipitates with a Ag-rich center and Cu-rich exterior were observed. None of the EDS analyses on the precipitates showed the presence of Mg.

An attempt was made to predict the precipitating phase for the 2195 alloy using a thermodynamic software called ThermoCalc® (Ref. 14) with an aluminum alloy database (Ref. 15). These calculations considered the Al, Cu, Mg and Zr elements and the phase equilibrium between Al_2CuMg, Al_3Zr, Al_2Cu, Al_3Mg_2, liquid and FCC solid solution. Since there are no thermodynamic data on the metastable T1 and other precipitates, they were not included in the analysis. The equilibrium calculations for the alloy composition Al-4.0 wt-% Cu-0.5% Mg-0.1% Zr were performed as a function of temperature and the results are presented in Fig. 7. The results show the predominant second-phase precipitates will be Al_2Cu, Al_2CuMg and Al_3Zr at low temperatures. But, at around 400°C, only Al_2Cu will be the stable precipitate and the volume percentage will be 3.3% (4.7% wt-%). The calculations qualitatively agree with the measured precipitate volume percentage and type observed in thermal cycled samples.

These observations suggest the softening observed in the TC1 condition may be due to many competing mechanisms.

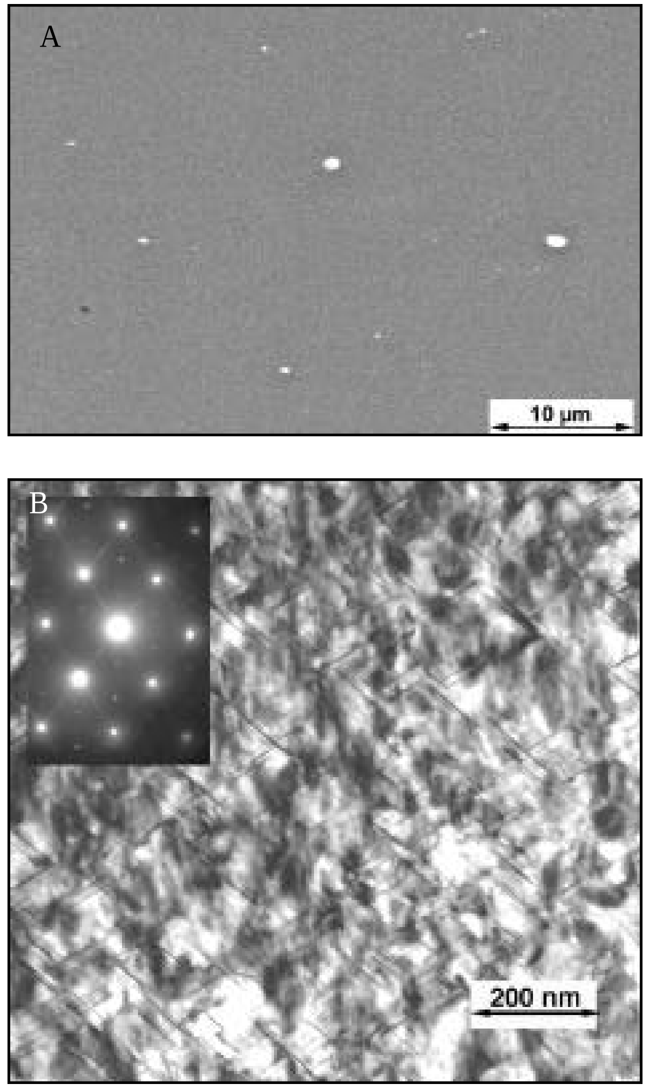

Fig. 2 — Characterization of base metal microstructure: A — SEM backscattered electron image showing the presence of Cu-rich and Cu- and Fe-rich particles; B — transmission electron micrograph with electron diffraction indicating the presence of T1 precipitates.

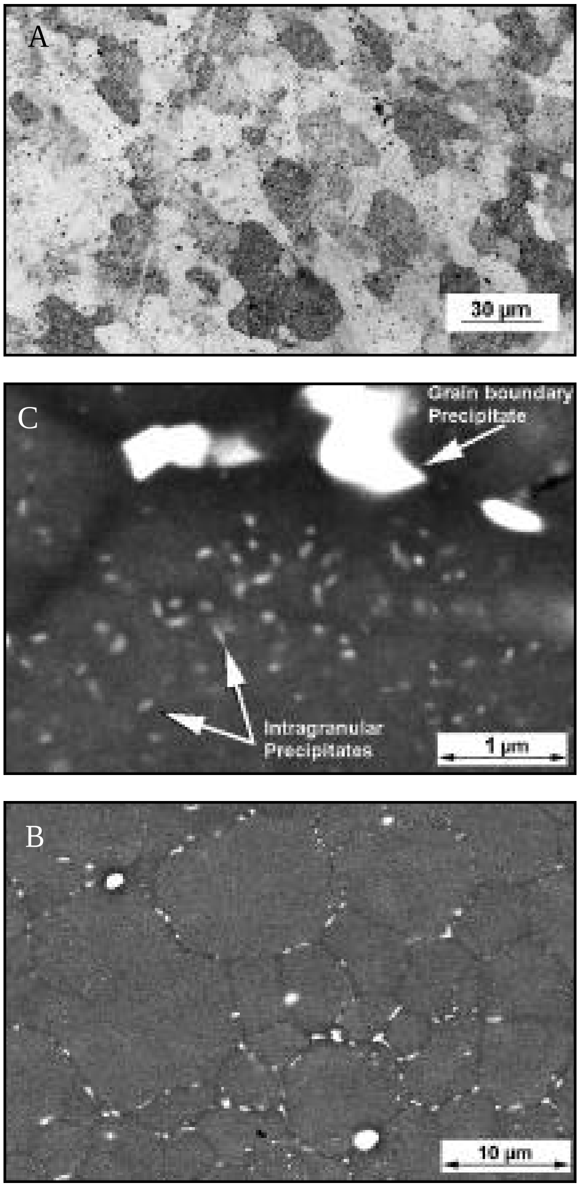

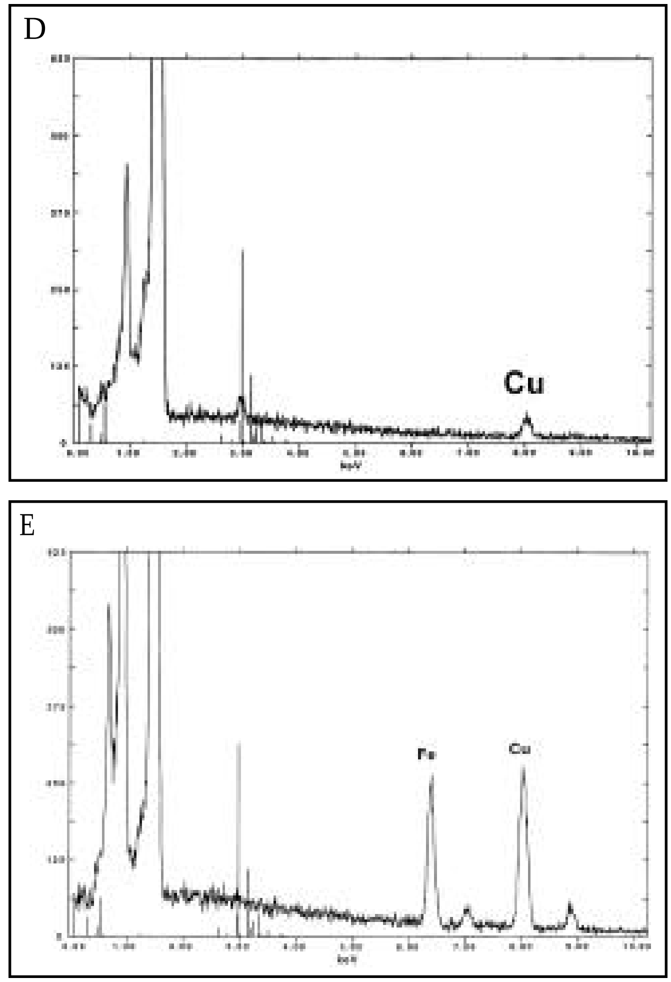

Fig. 3 — Detailed analysis of the weld DXZ: A — Optical micrograph shows equiaxed grain structure; B — backscattered electron SEM image shows the presence of large grain boundary precipitates; C — small rod-/disklike intragranular precipitates; D — the EDS spectrum obtained from the matrix shows the presence of copper; E — similar analysis from the grain boundary precipitates shows the presence of copper and iron.

Essentially, the strength of the aluminum alloy can be factorized into different parameters as given in the following:

$$Strength = \sigma_{int} + \sigma_{solid\ solution} + \sigma_{ppt} + \sigma_{dislocation} + \sigma_{grain\ size} \qquad (1)$$

In the above expression, σ_{int} corresponds to the intrinsic strength of an aluminum alloy, $\sigma_{solid\ solution}$ is the strength contribution due to solid solution, σ_{ppt} is the strengthening due to age-hardening precipitates, $\sigma_{dislocation}$ is the strengthening due to dislocation content and $\sigma_{grain\ size}$ is the contribution from the grain size variation. All of these components may operate in the age-hardening alloy subjected to thermomechanical deformation. Each component in turn depends on other variables such as alloying element concentration, precipitate volume fraction, dislocation density and grain size. With known relations (Ref. 16), Equation 1 can be converted to the following form:

$$Strength = \sigma_{int} + \sum_{i=1}^{n} k_i e_i + k_{ppt}\left(f_{ppt}\right)^m + k_{dislocation}\sqrt{\rho} + \frac{k_{grain}}{\sqrt{d}} \qquad (2)$$

where k_i corresponds to the coefficient of solid-solution hardening, e_i is the concentration of each alloying element, n is the number of alloying elements, k_{ppt} is the coefficient of hardening due to precipitation, f_{ppt} is the volume fraction of precipitates, m is the power constant for precipitate hardening, ρ is the dislocation density, $k_{dislocation}$ is the coefficient for dislocation hardening that is related to shear modulus, k_{grain} is the coefficient for grain size effect and d is the grain diameter. It is also important to note that in polycrystalline materials, the hardening resulting from dislocations and finer grain size is related. Although it is difficult to evaluate all of the constants in Equation 2 for the alloy considered in this work, the effect of each parameter on overall strength can be evaluated qualitatively. In the as-welded condition, the microstructure contains fine grains (~10 µm) with large dislocation density, as well as recovered structure and small precipitates (10–50 nm) within the grain, and coarse precipitates along the grain boundaries. This condition will yield large strengthening characteristics and, as expected, the hardness in the DXZ region is high and is equivalent to that of base metal in the aged condition. It is important to note base metal strengthening is achieved because of fine metastable, semicoherent T1 and other precipitates,

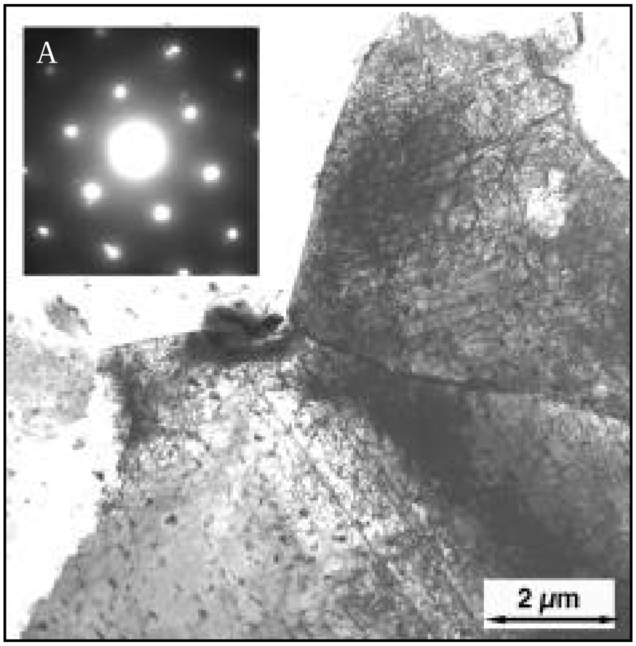

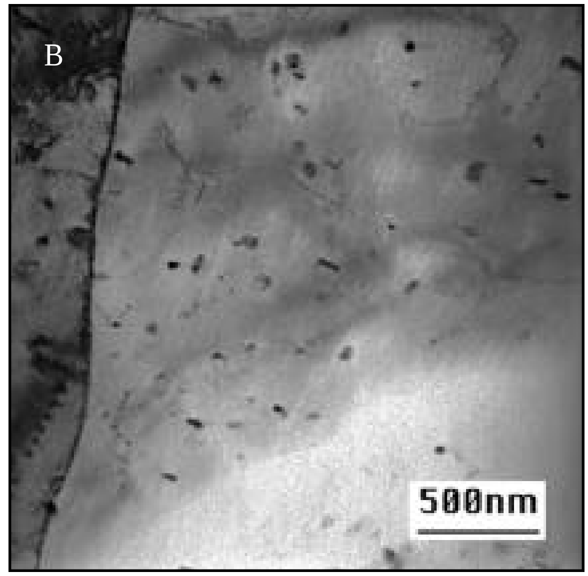

and the DXZ region does not contain these precipitates. On thermal cycling, the dislocation density decreases and volume fraction of other precipitates increases in the DXZ, leading to reduced strength levels. The precipitation reaction is expected to reduce the solid-solution hardening. There was no change in grain size during thermal cycling and, therefore, grain size contribution will remain the same. This suggests the precipitation during thermal cycling is insufficient to offset the drop in strength due to the reduction in dislocation and solid-solution hardening.

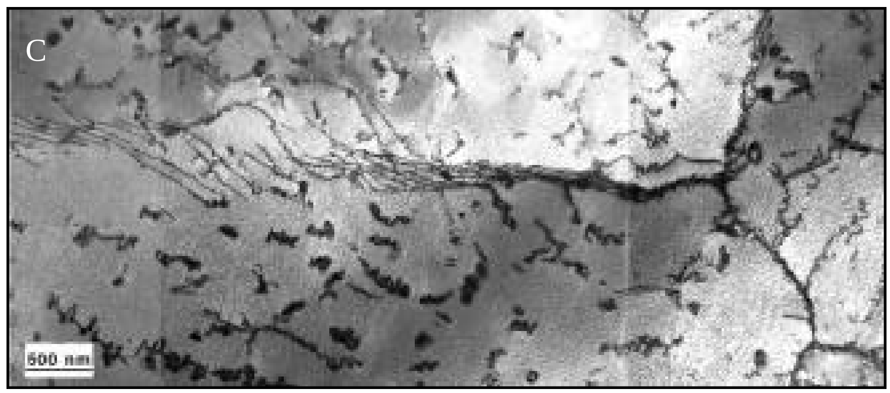

Fig. 4 — A — Detailed transmission electron microscopy of DXZ in the weld showing a grain with high dislocation density. The electron diffraction patterns indicate the absence of T1 precipitates. In addition, DXZ regions also showed the following: B — small Cu-rich precipitates (imaged off-zone) within the matrix; C — initial stages of a subgrain boundary formation.

Grain Growth Characteristics in the Weld Metal Region

In addition to precipitation reactions and the recovery process, it is important to consider grain growth characteristics of the DXZ region. The DXZ regions were subjected to grain growth experiments at 200, 300 and 400°C for various periods of time. The SEM backscattered electron images of microstructures from samples after 8 h at different temperatures are shown in Fig. 8. The micrographs show that, in addition to grain size changes, the precipitation characteristics also changed. With an increase in temperature, the grain boundary precipitation became more copious and the average size of the precipitates increased. This suggests these precipitates will influence grain growth characteristics. Grain size of these samples was measured using optical microscopy and manual tracing of grain boundaries. Typical grain structure traces from the as-welded condition and after 8 h at 400°C are compared in Fig. 9. These tracings were analyzed with the NIH image analyzer and grain size distributions were obtained. Interestingly, these data showed on aging at 200°C, the average grain size reduces. This is evident in the comparison of grain size distributions shown in Fig. 10. The distribution after 256 h of exposure at 200°C was skewed toward a smaller grain size compared to that of the as-welded condition. This could be related to the recrystallization of deformed grains present in the as-welded condition. The average grain size distribution from all temperatures is shown in Fig. 11. The results show the grain size increased without any initial decrease only at 400°C. The average grain size decreased initially at 300°C; above 2 h of exposure, the grain size increased. It is important to note the grain size changes shown in Fig. 11 are statistically significant, because they are based on a large number of grain samplings.

The grain growth equations with the influence of precipitates have been dealt with before (Ref. 17) and are expressed by the following equation:

$$d = \frac{r_{ppt}}{3f_{ppt}}\left(\frac{3}{2} - \frac{2}{Z}\right) \quad (3)$$

where r_{ppt} is the radius of the precipitate, f_{ppt} is the volume fraction of precipitate and Z is the ratio of maximum grain size to the average grain size. This grain size limiting relation will change with a change in f_{ppt} or r_{ppt}. In the present case of grain growth experiments at 200 and 300°C, in the initial stages the f_{ppt} is expected to increase and thereafter will remain constant. However, the change in r_{ppt} in the present case is expected to be

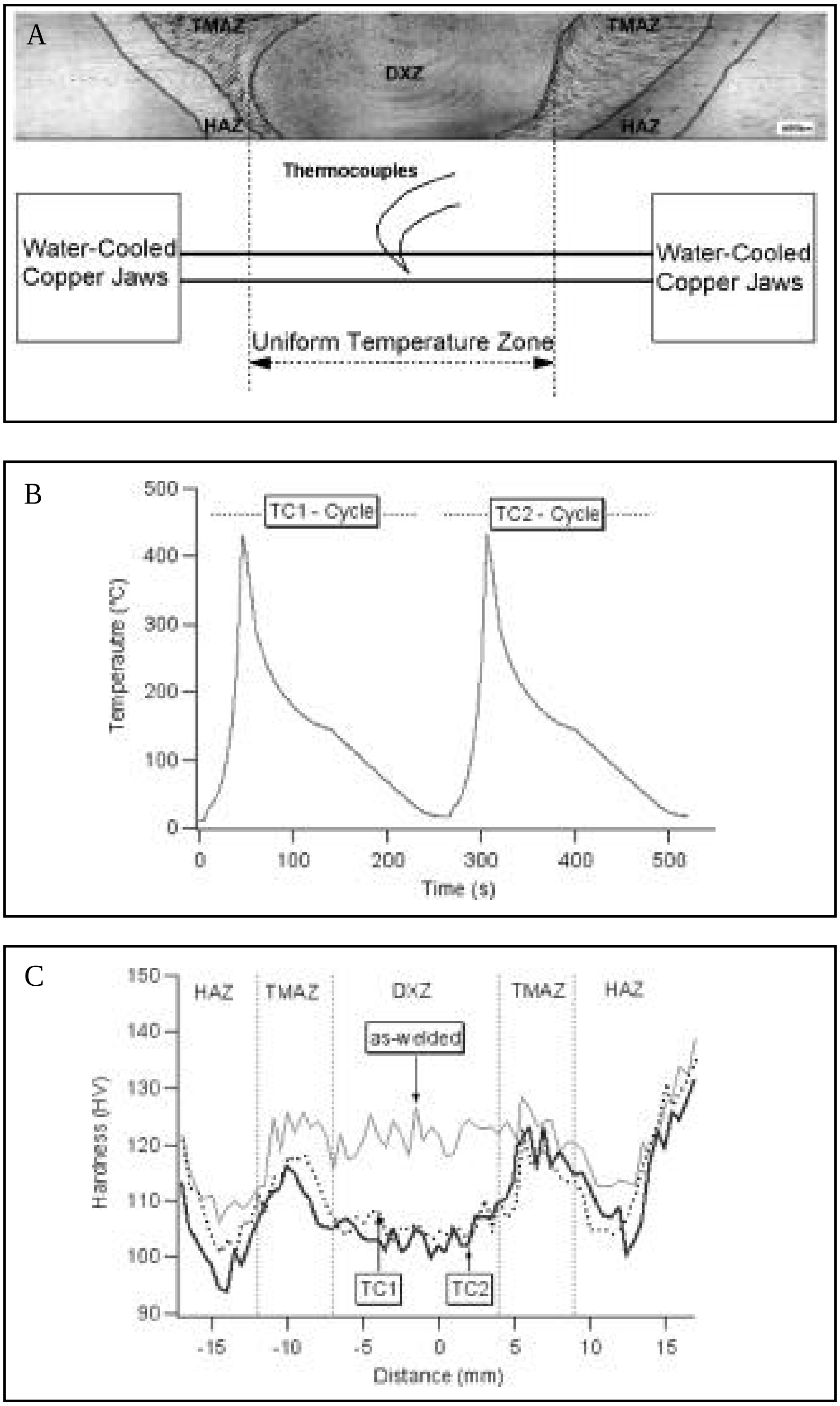

Fig. 5 — A — Geometry of the sample for thermal cycling; B — thermal cycles used in this investigation; C — comparison of hardness variations after thermal cycling conditions with the one measured from the as-welded condition. The regions corresponding to hardness distributions are also marked on the plot.

complex. This is because of the nucleation of small precipitates within the grain and along the grain boundary, as well as growth of existing coarse precipitates along the grain boundary. Therefore, there is a need to model these interactions between precipitation kinetics (change of f_{ppt} and r_{ppt} with time) and grain growth behavior. Although Equation 3 suggests a possible decrease in limiting grain size due to interaction with a precipitation reaction, the reduction in grain size from the as-welded condition cannot be easily explained. The initial decrease in grain size may be attributed to the recrystallization of those grains that exhibited large dislocation density in the as-welded condition — Fig. 4A. In the case of grain growth at 400°C, the precipitation reaction and dissolving reaction may occur rapidly and the sample will reach the equilibrium fraction of precipitates. After this, the precipitates will undergo simple Ostwald ripening-type growth and will lead to an increase in grain size. Equation 3 will then hold well. These results and TEM observations (Fig. 4) suggest DXZ regions are not in a completely recrystallized state in the as-welded condition.

Summary and Conclusions

Microstructures of friction-stir-welded 2195 aluminum alloy were characterized in the as-welded, postweld thermal cycled and isothermally aged conditions. The as-welded microstructure consists of microstructure gradients, including a dynamically recrystallized zone, thermomechanically affected zone and a soft heat-affected zone. Transmission electron microscopy of the DXZ illustrated the absence of T1 precipitates and also the coexistence of recovered and heavily dislocated grains next to each other. EDS analysis identified the presence of small precipitates within the grain and along the grain boundaries that are either rich in copper alone or in both copper and iron.

After postweld thermal cycling, hardness in the DXZ decreased. Transmission electron microscopy of these samples revealed average dislocation density in these regions was qualitatively less than that in the as-welded condition. EDS analysis indicated the presence of small (<20 nm) precipitates containing silver, as well as composite copper-rich precipitates containing a silver-rich phase, along the grain boundaries. Transmission and scanning electron microscopy revealed the precipitate fractions increased with thermal cycling. These results show the matrix in the as-welded condition is supersaturated and that precipitates form within the grains and at grain boundaries during thermal cycling.

Grain growth kinetics of DXZ at 200°C indicated a small decrease in grain size as a function of time. However, as the temperature increased to 400°C, the grain size increased monotonously with time. This is related to competition between recrystallization of new grains, precipitation reactions and grain growth mechanisms.

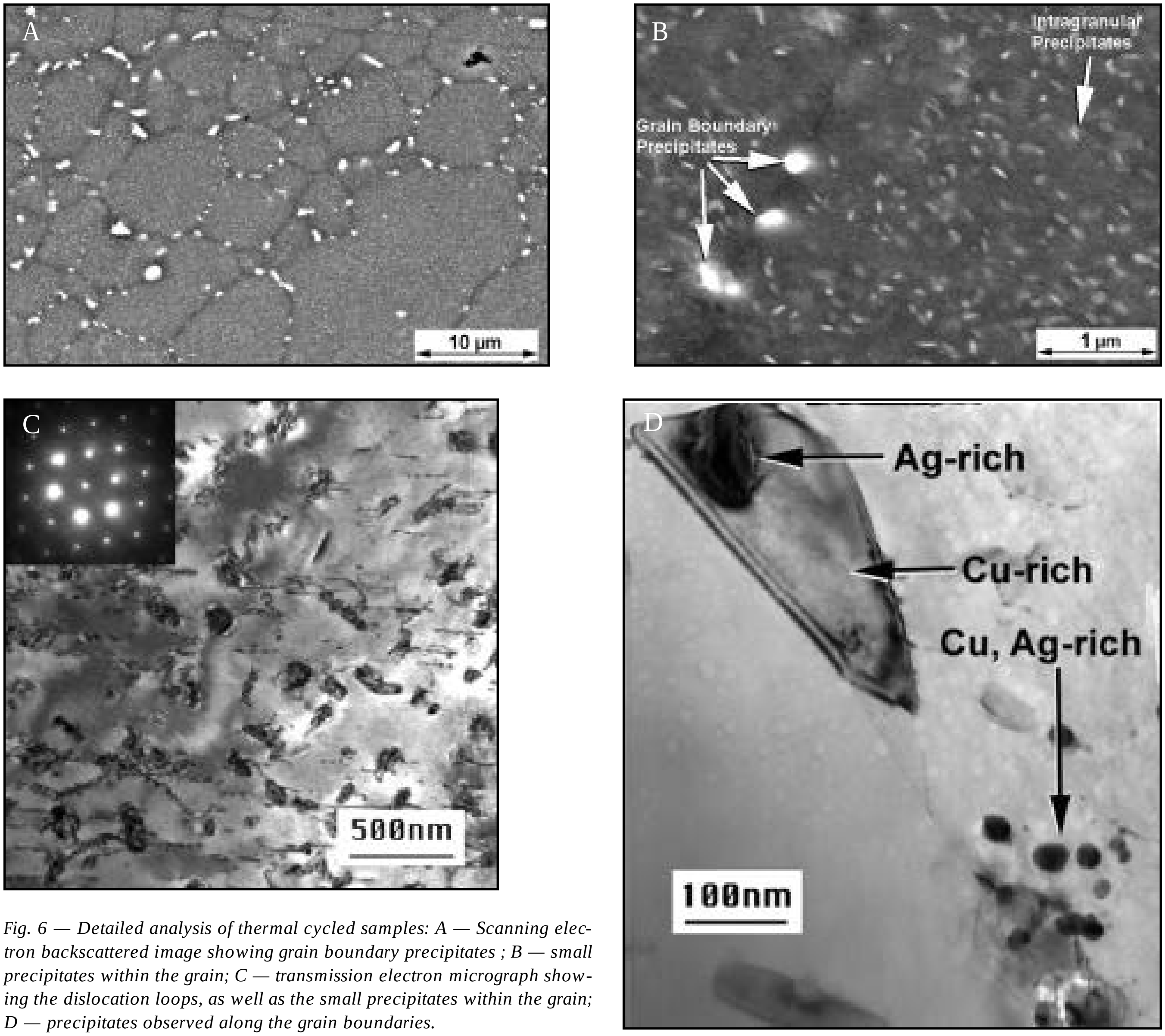

Fig. 6 — Detailed analysis of thermal cycled samples: A — Scanning electron backscattered image showing grain boundary precipitates ; B — small precipitates within the grain; C — transmission electron micrograph showing the dislocation loops, as well as the small precipitates within the grain; D — precipitates observed along the grain boundaries.

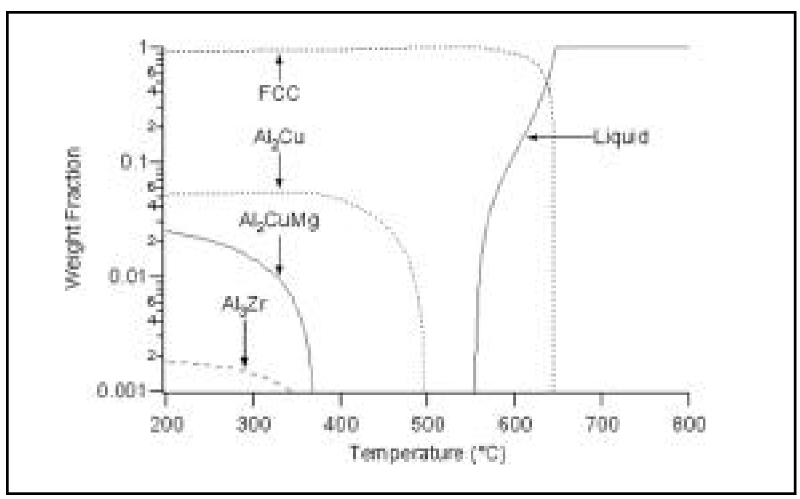

Fig. 7 — Predicted weight fractions of various phases calculated with ThermoCalc software as a function of temperature.

Acknowledgments

This research was sponsored by the Division of Materials Science and Engineering, U.S. Department of Energy, and Assistant Secretary for Energy Efficiency and Renewable Energy, Office of Industrial Technologies, Advanced Industrial Materials Program under contract DE-ACO5-00OR22725 with UT-Battelle and through the SHaRE Program under contract DE-AC05-76OR00033 with Oak Ridge Associated Universities. The authors thank William J. Abergast and Paula J. Hartley of Lockheed Martin Manned Space System Complex, New Orleans, La., for providing the welds used in this investigation.

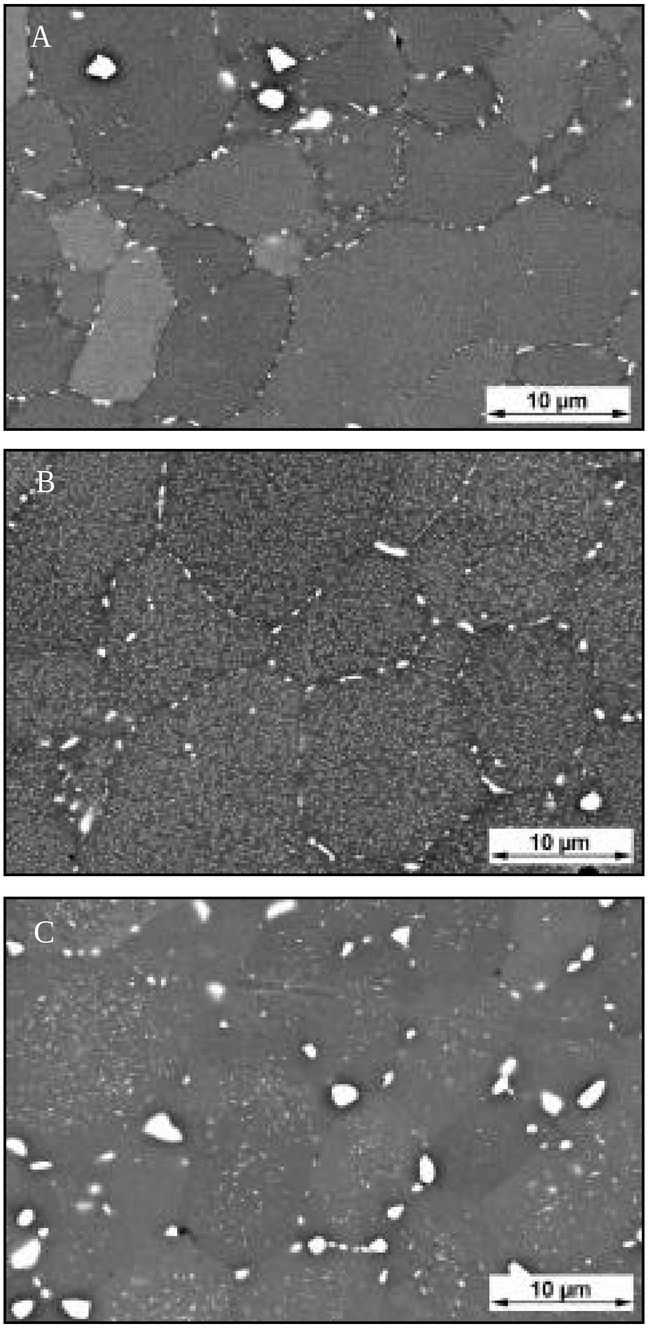

Fig. 8 — Scanning electron micrographs of DXZ after grain growth experiments: A — After 8 h at 200°C; B — after 8 h at 300°C; C — after 8 h at 400 °C.

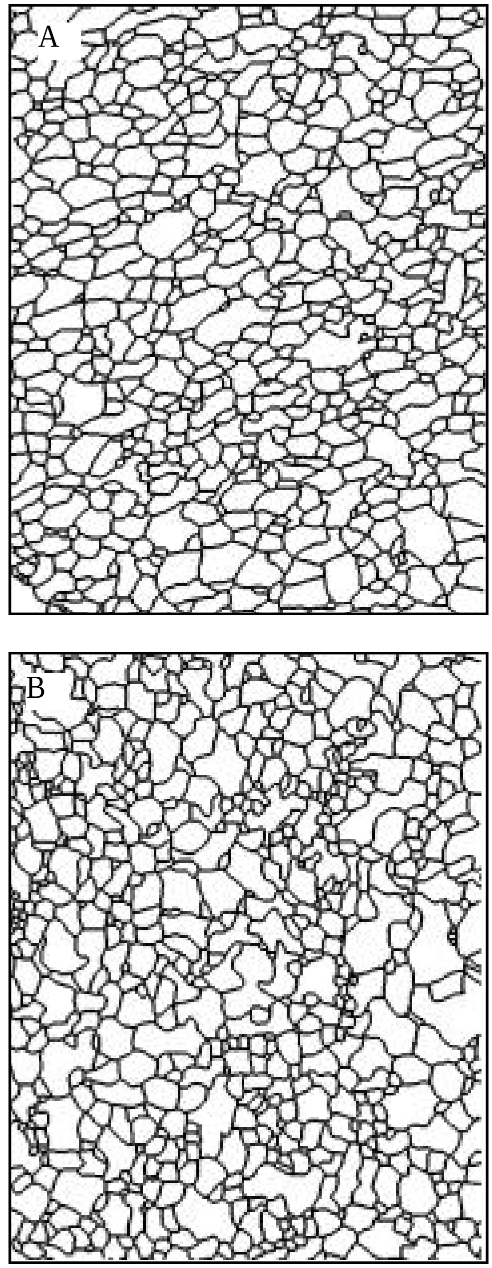

Fig. 9 — Typical grain growth profiles obtained from the optical micrograph samples: A — As-welded condition; B — 8 h at 400 °C.

References

1. Dawes, C. J. 1996, Friction stir welding of aluminum. *IIW-DOC XII-1437-96,* pp. 49–57.

2. Knipstorm, K. E. 1995. New welding method for aluminum. *Svetsaren* 50: 5–6.

3. Arbegast, W. J., and Hartley, P. 1999. Friction stir weld technology development at Lockheed Martin Michoud Space System — an overview. *Proc. Intl. Conf. on Trends in Welding Research*, eds. J. M. Vitek, S. A. David, J. A. Johnson, H. B. Smartt and T. DebRoy. ASM International, Materials Park, Ohio, pp. 541–546.

4. Waldron, D. J., Roberts, R. W., Dawes, C. J., and Tubby, P. J. 1999. Friction stir welding characterization for aerospace structures. *Ibid*, pp. 547–552.

5. Jones, III, C. S. 1999. Friction stir welding of large-scale cryogenic fuel tanks for aerospace applications. *Ibid*, pp. 553–557.

6. Li, Z. X., Arbegast, W. J., Hartley, P., and Meletis, E. I. 1999. Microstructure characterization and stress corrosion evaluation of friction stir welded Al-2195 and Al-2219 alloys. *Ibid*, pp. 568–573.

7. Mahoney, M. W., Rhodes, C. G., Flintoff, J. G., Spurling, R. A., and Bingel. 1998. Properties of friction stir welded 7075 T651 aluminum. *Metall. Mater. Trans. A.*, 29A: 1955–1964.

8. Sato Y. S., Kokawa, H., Enomoto, M., and Jogan, S. 1999. Microstructure evolution in 6063 aluminum during friction stir welding. *Metall. Mater. Trans A.*, 30A: 2429–2437.

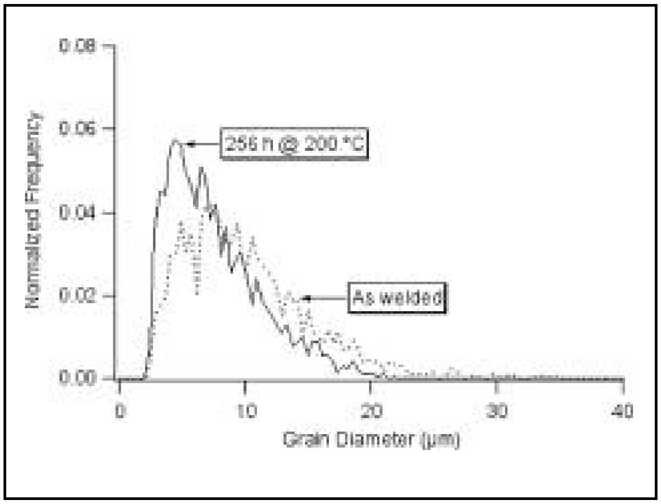

Fig. 10 — Comparison of grain size distribution obtained from the as-welded condition and that of 256 h at 200°C.

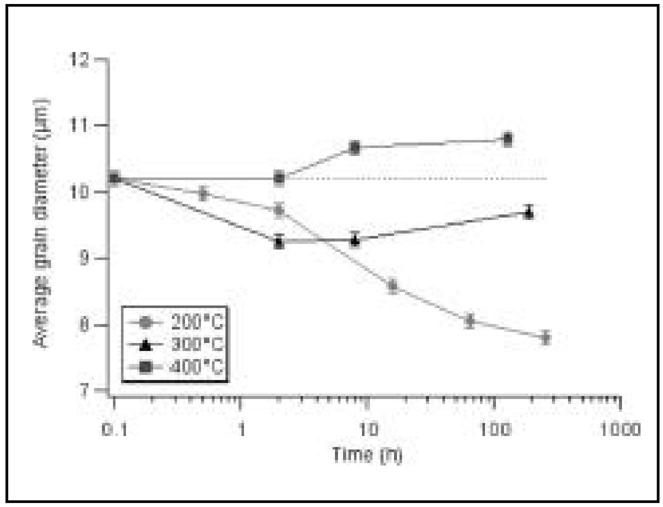

Fig. 11 — Grain growth kinetics as a function of temperature for the DXZ region of the weld. The error bars correspond to standard error of 0.1 µm.

9. Murr, L. E., Liu, G., and McClure, J. C. 1998. A TEM study of precipitate and related microstructures in friction-stir welded 6061 aluminum. *J. of Mater. Sci.* 33: 1243–1251.

10. Frankel, G. S., and Xia, Z. 1999. Localized corrosion and stress corrosion cracking resistance of friction stir welded aluminum alloy 5454. *Corrosion* 55: 139–150.

11. Diwan, R. M. 1994. Quantitative microstructural analysis and weldability study of aluminum lithium alloys. *Proc. Conf. on Metallographic Characterization of Materials Behavior. Microstructural Science* 21: 343–356.

12. Radhakrishnan, B., Sarma, G., and Zacharia, T. 1998. Monte Carlo simulation of deformation substructure evolution during recrystallization. *Scripta Metal.* 39: 1639–1645.

13. McClure, J. C., Tang, W., Murr, L. E., Guo, X., Feng, Z., and Gould, J. E. 1999. A thermal model of friction stir welding. *Proc. Intl. Conf. On Trends in Welding Research*, eds. J. M. Vitek, S. A. David, J. A. Johnson, H. B. Smartt and T. DebRoy. ASM International, Materials Park, Ohio, pp. 590-595.

14. Sundman, B., Jansson, B., and Andersson, J. O. 1985. The Thermo-Calc databank system. *Calphad* 9: 153–190.

15. Saunders, N. Al-data information. ThermoTech Ltd., Guildford, Surrey, U.K.

16. Dieter, G. E. 1981 *Mechanical Metallurgy*. New York, N.Y.: McGraw Hill.

17. Martin, J. W., and Doherty, R. D. 1976. *Stability of Microstructures in Metallic Systems*. Cambridge Solid State Science Series, University Press, Cambridge, U.K.